This is a pre-print of an article published in Journal of Paleolimnology. The final authenticated version is available online at: https://doi.org/10.1007/s10933-018-0028-x

A high-resolution pigment and productivity record from the varved Ponte Tresa basin (Lake Lugano, Switzerland) since 1919: insight from an approach that combines hyperspectral imaging and high-performance liquid chromatography

A high-resolution pigment and productivity record from the varved Ponte Tresa basin (Lake Lugano, Switzerland) since 1919: insight from an approach that combines hyperspectral imaging and high-performance liquid chromatography

*Tobias Schneider[1, 2], Denise Rimer[2], Christoph Butz[1, 2], Martin Grosjean[1, 2]

1 Oeschger Centre for Climate Change Research, University of Bern, 3012 Bern, Switzerland
2 Institute of Geography, University of Bern, Erlachstrasse 9a, 3012 Bern, Switzerland

*Corresponding author: Tobias Schneider, Institute of Geography, University of Bern, Switzerland,
tobias.schneider@giub.unibe.ch

Received: 7 November 2017 / Accepted: 26 March 2018; doi: https://doi.org/10.1007/s10933-018-0028-x

Key words: Eutrophication; Global change; Paleolimnology; Freshwater systems; Anthropocene; Alps

Abstract
Eutrophication, prompted by anthropogenic activities and climate change has led to multiple adverse effects in freshwater systems across the world. As instrumental measurements are typically short, lake sediment proxies of aquatic primary productivity (PP) are often used to extend the observational record of eutrophication back in time. Sedimentary pigments provide specific information on PP and major algal communities, but the records are often limited in the temporal resolution. Hyperspectral imaging (HSI) data, in contrast, provide very high seasonal (sub-varve-scale) resolution, but the pigment speciation is limited.
Here, we explore a combined approach on varved sediments from the Ponte Tresa basin, southern Switzerland, taking the advantages of both methods (HSI and high performance liquid chromatography, HPLC) with the goal to reconstruct the recent eutrophication history at seasonal to interannual resolution. We propose a modified scheme for the calibration of HSI data (here: Relative Absorption Band Depth between 590 and 730 nm $RABD_{590\text{-}730}$) and HPLC-inferred pigment concentrations (here: 'green pigments' {chlorophyll *a* and pheophytin *a*}) and present a calibration model (R^2= 0.82; RMSEP ~ 12%). The calibration range covers >98% of the spectral index values of all individual pixels (68 µm x 68 µm) in the sediment core. This allows us to identify and quantify extreme pigment concentrations related to individual major algal blooms, to identify multiple algal blooms within one season, and to assess interannual variability of PP.
Prior to the 1930s, 'green pigment' concentrations and fluxes (~50 µg g^{-1}; ~2 µg cm^{-2} a^{-1}, chlorophyll *a* and pheophytin *a*) and interannual variability was very low. From the 1930s to 1964, chlorophyll *a* and pheophytin *a* increased by a factor of ~4, and *ββ*-carotene appeared in substantial amounts (~0.4 µg cm^{-2} a^{-1}). Interannual variability increased markedly and a first strong algal bloom with 'green pigment' concentrations as high as 700 µg g^{-1} is observed in 1958. Peak eutrophication (~12 µg cm^{-2} a^{-1} chlorophyll *a* and pheophytin *a*) and very high interannual variability with extreme algal blooms ('green pigment' concentrations up to 1400 µg g^{-1}) is observed until ca. 1990, when eutrophication decreases slightly. Maximum PP values after 2009 are likely the result of internal nutrient cycling related to repeated deep mixing of the lake.

8.1 Introduction

Eutrophication of freshwater systems is recognized as one of the most relevant environmental problems and has been observed across the world (Friedrich et al. 2014; Jenny et al. 2016). Adverse effects include, among others, harmful algal blooms (Lee et al. 2016), enhanced stratification (Boehrer and Schultze 2008), anoxia in bottom waters and fish kills. These impacts put lacustrine ecosystems, biodiversity and related ecosystem services at risk (Mills et al. 2017). In most systems, eutrophication emerged as a problem in the 20th century due to a combination of anthropogenic activities, in particular nutrient loads (Battarbee et al. 2012; Jenny et al. 2016; Mills et al. 2017) and climate change (Lee et al. 2016). In some parts of the world, anthropogenic eutrophication started as early as at the end of the 19th century (Smith 1998). Awareness increased and the problem became widely recognized in the 1960s (Battarbee et al. 2012). In the following years, restoration measures (e.g. sewage treatment plants or limitation of fertilizer in agriculture) were implemented to reduce external P-loads and to improve

water quality and lake ecosystems (Aeschbach-Hertig et al. 2007). To evaluate the success of lake restoration measures, to assess conditions prior anthropogenic impact and to set reasonable management targets, long series of observational data are needed but often not available (Hall et al. 1997; Jenny et al. 2016; Mills et al. 2017).

Lake sediments record the development of nutrient cycling and productivity and, thus, provide empirical evidence for eutrophication on long time-scales (Das et al. 2005; Battarbee et al. 2012; Mills et al. 2017). Varved (annually laminated) sediments are particularly valuable, because their formation is often indirect evidence for eutrophication (Jenny et al. 2013) and varves permit precise dating of changes observed in the sediment records (Zolitschka et al. 2015). This is important to detect eutrophication, attribute eutrophication to forcing factors, and to assess the efficiency or time-lags of particular restoration measures (Blass et al. 2007).

Several sedimentary proxies have been used to reconstruct eutrophication such as biogenic silica (Conley and Schelske 2002), diatom assemblages (Hall et al. 1997), total organic carbon or C isotopes (Meyers 1994; Dean 1999) and sedimentary pigments (Sanger 1988; Airs et al. 2001; Korhola et al. 2002; Leavitt and Hodgson 2002; Das et al. 2005; Reuss et al. 2005; Guilizzoni et al. 2011; Michelutti and Smol 2016 and others). If conditions for preservation in the sediment are suitable (Sanger 1988), pigments provide very specific information on major algal groups, including those that are typically not preserved as microfossils, and have shown to be a reliable proxy for past eutrophication.

The analysis of sedimentary pigments (typically with HPLC) is, however, challenging and high-resolution long records are difficult to obtain. Recently, important advancements have been made with non-destructive scanning reflectance spectroscopic techniques which facilitated the measurement of lutein, chlorophylls and their derivates (chlorins) directly from fresh sediment cores at mm-scale resolution (Rein and Sirocko 2002; Rein et al. 2005; von Gunten et al. 2009; Saunders et al. 2012; Amann et al. 2014). Butz et al. (2015) and Butz et al. (2017) developed this approach further and used spectra from a scanning hyperspectral imaging system (HSI; pixel size: ~68 x 68 µm; spectral resolutions ~2.7 nm) to infer 'green pigments' {chlorophyll *a* and pheophytin *a*} as well as bacteriopheophytin *a* at subvarve-scale resolution. The advantage of hyperspectral data is the very high spatial resolution; the disadvantage is that the speciation of the pigments is limited. Although the potential of hyperspectral imaging has been recognized (Croudace and Rothwell 2015), the method is still in its infancy and further applications in different sedimentary environments and for different scientific questions are needed to establish the method.

In the present study, we explore a combined approach using HSI and HPLC techniques to identify sedimentary pigments and reconstruct historic eutrophication in the Ponte Tresa basin, Lake Lugano (southern Switzerland) at seasonal and interannual resolution. A particular focus is placed on the question whether individual short-lived algal blooms can be detected by high-resolution HSI techniques. On the methodological side, we aimed at improving the calibration of hyperspectral data (spectral indices) with HPLC inferred pigment speciation and concentrations following a new scheme.

We have chosen the Ponte Tresa basin because the sediments of the 20th century are varved (Züllig 1982; Niessen 1987), the eutrophication signal is very pronounced and the eutrophication history is already well documented (Züllig 1982; Barbieri and Simona 2001; Lepori and Roberts 2017), thus providing an ideal testbed for our method.

8.1.1 Site description

The Ponte Tresa basin (45°58'N; 8°52'E; Fig. 8.1) is the westernmost part of Lake Lugano in the southern Swiss Alps. It is a fluvio-glacial tectonic lake that was shaped by the Adda and Ticino glaciers during the Pleistocene (Simona 2003). The bedrock of the watershed consists mostly of calcareous rocks and outcrops of porphyry and gneiss (Salmaso et al. 2007). The surface of the Ponte Tresa basin is ~1.1 km^2 and its direct watershed covers ~5.6 km^2 (Simona 2003). The maximum water depth is ~51 m, the volume amounts to 0.03 km^3, and the mean water residence time is ~0.04 years (Simona 2003). The Osgood Index ($OI = Z_{mean}/A^{0.5}$) of 31.5 suggests that periodic meromixis is likely (Huser et al. 2016). The most recent sediments are anoxic and varved (Züllig 1982; Niessen 1987). Lake Lugano is the main tributary of water and nutrients to the Ponte Tresa basin (Fig. 8.1a) and the Tresa River is the only outflow (annual discharge of ~0.75 km^3; Simona 2003). Mild winters, and warm and humid summers, characterize the regional climate (Niessen 1987). The steep slopes in the watershed are mostly covered by mixed deciduous forest, while dense settlements and industry dominate land cover in the lowlands and lake shore areas. The modern eutrophication history of Lake Lugano is well-

established (Barbieri and Simona 2001; Lepori and Roberts 2017). Early measurements of total phosphorus (TP) in Lake Lugano indicate the beginning of eutrophication in the 1940s. Due to urban and residential development and intensification of agriculture, TP concentrations in the water of the southern basin of Lake Lugano increased drastically in the 1960s, and peaked in the early 1980s with TP concentrations around 140 µg l^{-1}. The first of several sewage plants was built in 1969 and, in 1986, phosphorus was banned from detergents. From 1995 onwards, phosphorus was trapped in sewage treatment plants and lake water TP concentrations in the southern basin of Lake Lugano decreased to about 40 µg l^{-1} today (BAFU 2016).

However, Lake Lugano is still eutrophic today (Barbieri and Simona 2001; Lepori and Roberts 2017). Measurements in the Ponte Tresa basin of Lake Lugano (1972-1982) revealed that phosphate concentrations exceeded values of 400 µg l^{-1} and that conditions were mostly anoxic at the bottom of the lake (50 m) (IST-SUPSI 2016). In the lake's southern basin, summertime bottom water anoxia (O_2 <0.5 mg l^{-1}) still persists today, which is likely also the case in the Ponte Tresa basin (point measurements only). Veronesi et al. (2002) report on the importance of phosphorus with regard to aquatic primary production in the southern basin of Lake Lugano. In particular, they point to the role of P sedimentation, redox conditions and seasonal or episodic mixing regimes in the lake, all of which may lead to very efficient endogenic P cycling. Accordingly, primary production has not substantially decreased from peak values in the 1980s (C-flux about 377-469 g m^{-2} a^{-1}) and has remained high in recent years (C-flux around 340 g m^{-2} a^{-1}; IST-SUPSI 2016).

8.2 Methods

8.2.1 Fieldwork and sediment analyses

In July 2015, several short sediment cores were obtained from the depocenter of the Ponte Tresa basin by using a UWITEC gravity corer (coring site in Fig. 8.1b). Gas bubbles that formed while coring were removed with small perforations in the core liners. Additionally, we measured temperature, pH, specific conductivity, and dissolved oxygen (luminescence-sensor) with a Hydrolab MiniSonde-5 MS5 six times (10 second-intervals) per depth in consecutive 1 m steps across the depth profile.

8.2.2 Sedimentological and geochemical methods

Prior to opening, the sediment cores were scanned with a Multi-Sensor Core Logger (MSCL, Geotek) in 0.5 cm increments (Schultheiss and Weaver 1992). Thereafter, the cores were split lengthwise and the oxidized surfaces were described (Schnurrenberger et al. 2003). Firstly, we performed the non- destructive micro-x-ray fluorescence (µXRF) and hyperspectral imaging (HSI) techniques. Afterwards, one quarter of the sediment core was subsampled contiguously at 1 cm steps for geochemical analyses, and another quarter was subsampled contiguously at 2 cm for pigment analyses. The samples were stored in dark and frozen (-18°C) conditions before freeze drying.

X-ray radiographs were taken and semiquantitative elemental compositions were measured at 1 mm steps on the fresh sediment with a µXRF-scanner (ITRAX, Croudace et al. 2006) equipped with a Mo-tube (exposure time 20 seconds, 45 kV and 20 mA). In order to analyze sub-varve structures in the top sediment, a resin-embedded and polished sediment slab was additionally scanned at 0.2 mm resolution (Cr-tube, 20 seconds exposure time, 40 kV, 20 mA). B esides visual inspection, X-ray density data and selected µXRF elements (Si, K, Ti, Rb, Zr and Sr) were used to diagnose the two main sedimentary facies: (i) regular sedimentation of clastic-biogenic or biogenic varves (Zolitschka et al. 2015), and (ii) clastic event layers (Schillereff 2015). Using R statistical computing (R Core Team 2016), a principal component analysis (PCA) and a k-means cluster analysis were applied on the scaled (0-1), square-root transformed dataset. We chose a 'broken stick' approach to identify significant PCs (R-package "stats" v.3.2.5; R Core Team 2016). Silhouette plots (R-package "factoextra" v.1.0.4; Kassambara and Mundt 2017) supported the choice of numbers of k-means clusters (k=3). In Fig. 8.2a, the PC_1 (clastic layers) was colored according to the k-means clusters and plotted along a photo of the sediment core. Dry bulk density and water content were measured according to the method of (Håkanson and Jansson 2002). Total organic carbon (TOC) and inorganic carbon ($CaCO_3$) were determined by loss on ignition ($LOI_{550°C}$, $LOI_{950°C}$) as described in Heiri et al. (2001). To analyze biogenic silica (bSi), we followed the wet-alkaline method of (Ohlendorf and Sturm 2008). BSi and Al were measured by using ICP-OES (Agilent, VISTA AX).

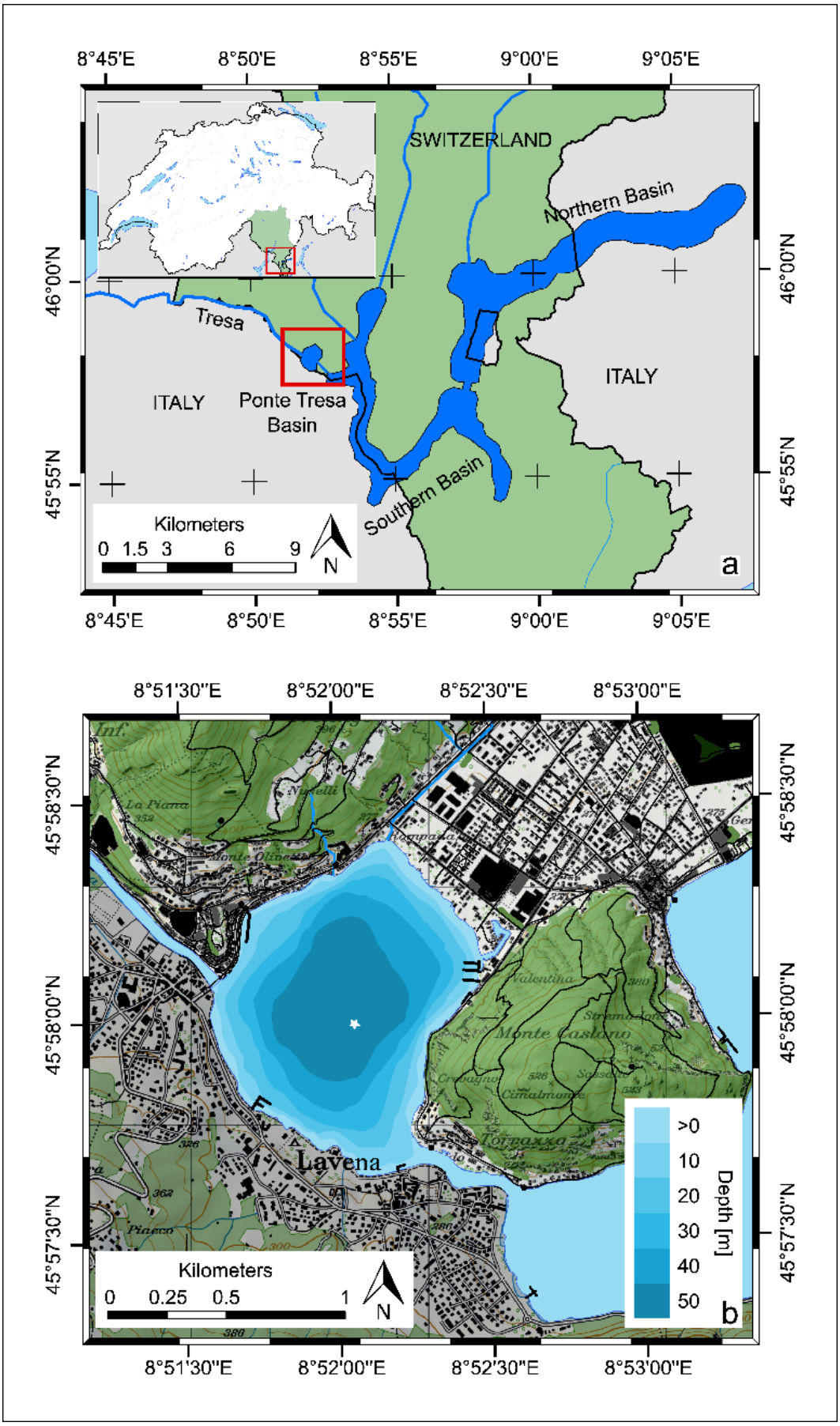

Fig. 8.1 Study site. (a) The small box in the top left corner shows Switzerland. Lake Lugano is shown in dark blue color. The red rectangle highlights the Ponte Tresa basin. (b) Bathymetry-map of the Ponte Tresa basin (adapted from Nordmeyer et al. 1978). The white asterisk indicates the coring site.

Using the method described by Kamatani and Oku (2000), we applied a 1:1 aluminosilicate-correction for lithogenic Si. The residual after bSi leaching was used for grain size analysis with laser diffraction (Malvern Mastersizer 2000).

8.2.3 Hyperspectral imaging and calibration

Following the approach of Butz et al. (2015), the half cores were scanned with the Specim Ltd. single core scanner equipped with a visual to near infrared range (VNIR, 400-1000 nm) hyperspectral linescan camera (Specim PFD-CL-65-V10E). We normalized the raw scans with a $BaSO_4$ white reference plate and extracted spectral endmembers according to the method of Kruse et al. (1999) by using the spectral hourglass wizard of the software ENVI 5.03 (Exelisvis ENVI, Boulder, Colorado). Based on the spectral endmembers, we calculated the relative absorption band depths (RABD) for an absorption feature between the reflectance at the wavelengths R_{590} and R_{730} (590-730 nm). In contrast to Butz et al. (2015), who used a fixed band for the trough minimum, we used here the local minimum of the absorption feature for each individual spectrum (i.e. each pixel individually, spatial resolution 68 µm x 68 µm). This approach ensures that small spectral shifts of the trough minimum are correctly addressed. Therefore, we used the following formula for RABD calculation (Eq. 1):

$$RABD_{590-730}=\left(\frac{X*R_{590}+Y*R_{730}}{X+Y}\right)/R_{localtroughmin} \quad [\text{Eq. 1}]$$

where RABD refers to the relative absorption band depth and R_λ to the reflectance at the wavelength (λ). X denotes the number of spectral bands between R_{730} and the trough minimum, and Y denotes the spectral band number between trough minimum and R_{590} (e.g. for a trough minimum at R_{690} X equals 51 bands and Y equals 126).

To convert the semi-quantitative HSI-index into absolute sedimentary 'green pigment' concentrations (here: chlorophyll *a* + pheophytin *a*), we followed a modified calibration method from Butz et al. (2017). Based on the assumption that the depth of the absorption feature at $R_{590\text{-}730}$ under the sensor field is related to the abundance of sedimentary (green) pigments, we used the image of the $RABD_{590\text{-}730}$ index values to determine the optimal regions for sediment sampling (used afterwards for pigment extractions and HPLC measurements for calibration). We chose the sampling regions such that the range and distribution of sediment subsamples used for calibration covered most of the gradient of the hyperspectral index values of the entire sediment core. In contrast to Butz et al. (2017), who used sediment samples encompassing several varves, the varve thickness in Ponte Tresa basin enabled us to sample individual seasonal sediment layers with very high pigment concentrations and, thus, to calibrate the uppermost range of the spectral index values. Finally, we applied a linear regression model between $RABD_{590\text{-}730}$ (HSI) and 'green pigment' concentrations (HPLC).

8.2.4 Sedimentary pigment analysis

Sedimentary pigments were extracted from the freeze-dried sediment as described in Amann et al. (2014). The extracts were dissolved in methanol (1 ml), after drying under a nitrogen stream, and 100 µl aliquots were injected into a HPLC (Agilent, infinity series 1200) equipped with a Waters Spherisorb ODS-2 column (5 µm, 250 x 4.6 mm), a diode array detector (190-640 nm), and a fluorescence-luminescence detector. The solvent mixtures and the solvent gradient followed Amann et al. (2014; modified after Airs et al. 2001). Selected major pigment species (chlorophyll *a*, chlorophyll *b*, pheophytin *a*, pheophytin *b* and *ββ*-carotene) were quantified based on a calibration with certified pigment standards. The interpretation model of the pigment groups followed Swain (1985), Lami et al. (2000), Leavitt and Hodgson (2002): (1) Chlorophyll *a* and pheophytin *a* (degradation product of chlorophyll *a*) are used as a proxy for phototrophic green algae. (2) Chlorophyll *b* and pheophytin *b* can reflect lacustrine (*Euglenophyta* and *Chlorophyta*) and/or terrestrial sources. (3) *ββ*-carotene is interpreted as a proxy of total algal biomass. (4) The ratio between total carotenoids (TC; here *ββ*-carotene) and chlorophyll derivates (CD; here pheophytin *a*) is used as a proxy for major algal compositions: high TC/CD ratios reflect high NPP, low oxygen-concentrations in bottom waters and dominance of blue-green algae.

Significant changes and zones in the pigment-stratigraphy were identified by a constrained incremental sum of squares clustering (CONISS, Grimm 1987; R-package "rioja", Juggins 2017). The number of clusters was determined with a broken stick model. Pigment-fluxes (µg cm^{-2} yr^{-1}) were calculated by multiplying the mass accumulation rate (g cm^{-2} yr^{-1}) times the pigment concentration (µg g^{-1}).

8.2.5 Chronology

Varve counting was conducted visually on high-resolution pictures of the oxidized sediment core surface using CooRecorder v.2.3 software (Larsson 2003). The light $CaCO_3$ summer layers (Niessen 1987) served as first-order counting criterion of the varves. In addition, we used Ca peaks inferred from µXRF data.

Prominent clastic layers (PC_1), previously identified as flood layers (Niessen 1987), were used to constrain the varve chronology (Fig. 8.3). Here, we used the historically documented floods of 1951, 1960, 1983 and 2002 (Palmisano 2008). The final chronology was composed from independent visual varve counts by three analysts, and one count which was based only on XRF data. The uncertainty calculation followed Tylmann et al. (2016), whereby the counting uncertainty was always reset to zero at each chronostratigraphic marker layer (documented flood). In contrast to Tylmann et al. (2016), our final uncertainty counts between the flood layers was calculated as the average from both counting directions (top-down and bottom-up).

The data used to prepare Figs. 8.4, 8.5 and 8.6, and ESM Figs. 8.1, 8.2 and 8.3 are archived at the University of Bern data repository BORIS: https://boris.unibe.ch/

8.3 Results

8.3.1 Sediment stratigraphy

The sediment description and the PCA discrimination consistently revealed that the uppermost ~84 cm of the sediments in Ponte Tresa (Fig. 8.2a) are composed of two facies.

Facies 1 consists of variably thick varves (0.2 cm to ~1.2 cm). The finest laminations are found between the core bottom at 83 cm and ca. 44 cm depth. The sediment is relatively low in TOC (3 % to 7 %) and is brighter in color varying between yellowish gray (Munsell 2.5Y 4/1) and gray (Munsell 5Y 5/1). Relatively low CaCO3 concentrations (3-10 %) and low water contents (68-75 %) point to rather minerogenic sediments deposited in mesotrophic lake conditions (ESM Fig. 8.1). Slightly thicker biogenic varves are present from 44 cm to the clastic layer at ~33 cm depth. The colors of these organic silty clay laminae range from yellowish-gray (Munsell 2.5Y 5/6) to dark olive (Munsell 5Y 4/3). This section is characterized by slightly higher TOC (around 7 %), higher CaCO3 (6-16 %), and higher water content (75-82 %) compared to the sediment below. The thickest biogenic varves are found in the top section (33 cm to 0 cm). The dark laminations consist of light olive brown (Munsell 2.5Y 5/4) to grayish olive (Munsell 5Y 5/3) silty clays. Total organic carbon (TOC) averages ~8.5 %, CaCO3 is ~14 % and water content is ~78.5 % (ESM Fig. 8.1).

Facies 2 includes discrete massive clastic layers up to 1.5 cm thick (e.g. at 32 cm sediment depth, Fig. 8.2a). Compared with Facies 1, these layers are depleted in TOC (~3 %), CaCO3 (~4 %) and show a low water content (~50 %; ESM Fig. 8.1). The colors of the clastic layers are distinctly different from Facies 1 and vary between dark grey (Munsell 2.5Y 4/1) and pale olive (Munsell 5Y 6/3). PC1 (76.1%, Fig. 8.2b) reveals that the clastic layers are all enriched in Zr, Rb, Ti, K and Si (Fig. 8.2c, brown points in Fig. 8.2b), hence, supporting the discrimination between Facies 1 and Facies 2.

The close-up of the top 12 mm of the sediment (three varve years 2012-2015; Fig. 8.2d) reveals a cyclic succession of composition from bottom to top. The cycle begins with a peak in green pigments ($RABD_{590-730}$) followed closely by a relative maximum in Ca that is finally followed by a peak in Ti. The $RABD_{590-730}$ maxima show peaks in chlorophyll a related pigments ('green pigments') and are interpreted as the spring algal bloom. The $RABD_{590-730}$ maxima coincide often with Si maxima, suggesting that biogenic provenance of Si (diatoms) is substantial. In the absence of green pigments, Si peaks coincide with Ti maxima (e.g. winter 2014). Ca peaks are interpreted as authigenic CaCO3 precipitation in early summer, which is related to epilimnetic warming and increased primary production after spring mixing. Finally, the Ti peaks are interpreted as winter layers at times of low authigenic calcite and biomass production and increased loads of suspended sediment entering the lake. Secondary $RABD_{590-730}$ maxima within one 'green pigment'- Ca-Ti cycle are interpreted as multiple algal blooms in the same year.

8.3.2 Varve chronology

Authigenic CaCO3 layers, the first-order criterion used for varve counting, were well identifiable in the top sediments down to a depth of 44 cm. Further down (45 – 84 cm), in the less organic and more clastic part of the sediment core, calcite layers were difficult to identify, and layer counting was ambiguous. Therefore, our varve chronology (Fig. 8.3) begins at 44 cm sediment depth with a varve age of 1919 (+0/-10). Extrapolation of the age-depth model suggests an age of approximately 1800 at 83 cm sediment depth. Between 1951 (i.e. the first chronostratigraphic marker) and 1983, the age uncertainty decreases to +1/-4 years. In the uppermost section (1983 – 2015), counting uncertainty is +1/-1 year. According to the age-depth model, the sediment mass accumulation rate MAR of Facies 1 (varved sediments) is relatively constant at around 30 mg cm-2 a-1. Sediment sections with clastic event layers show higher MAR values (~40 mg cm-2 a-1).

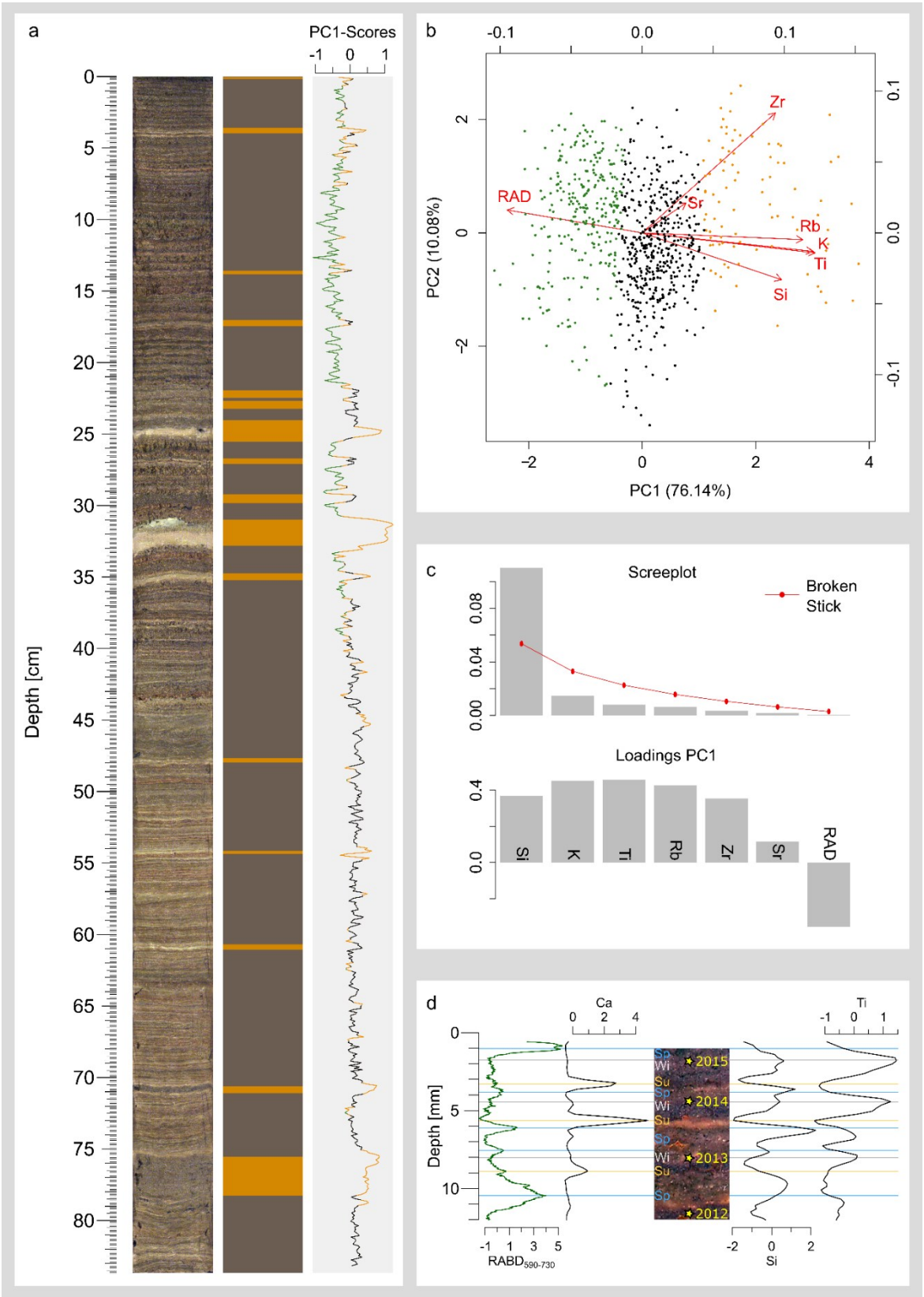

Fig. 8.2 showing the core of Ponte Tresa, the statistical flood-layer discrimination and a close up of 4 varves are shown. (a) The RGB contrast enhanced core picture (left), a pictograph from the visual Facies classification (orange colors highlight the flood-layers of Facies 2) and the PC1 (colored according to the k-means clusters; orange cluster: clastic layers, black cluster: mixed layers, green cluster: organic sediments mostly Facies 1). RAD stands for χ-Ray counts (the less counts, the denser the material). The biplot (b), screeplot and the loadings (c) of the PCA are shown on the right. (d) Close up of four varve years made on a resin-embedded sediment block. The annual varve cycles (Sp: Spring; Su: Summer; Wi: Winter) are indicated with differently colored lines. XRF-data plots can be found in ESM Fig. 2.

8.3.3 Spectral index $RABD_{590\text{-}730}$, calibration and downcore measurements

The calibration of the HSI index (RADB590-730) with absolute green pigment concentrations (chlorophyll *a* + pheophytin *a*) as determined by HPLC resulted in a Pearson correlation of r= 0.91 ($p<0.001$) and a coefficient of determination of R2adj= 0.82 ($p<0.001$; Fig. 8.4a). The positions of the 31 sediment samples used for the calibration is marked in Fig. 8.5 (black arrows). The root mean squared errors of prediction (RMSEP) vary between 122.64 µg g^{-1} (k-fold) and 129.98 µg g^{-1} (bootstrapped), which corresponds to an uncertainty of ~12%. The calibration covers a broad range from minimum values ($RABD_{590\text{-}730}$ = 1.05; {chlorophyll *a* + pheophytin *a*} = 2.80 µg g^{-1}) to maximum values ($RABD_{590\text{-}730}$ = 2.0; {chlorophyll *a* + pheophytin *a*} = 1051.9 µg g^{-1}) thus encompassing > 98 % of all $RABD_{590\text{-}730}$ index values measured along the core (Fig. 8.5). Residual analysis revealed that the two outlier samples (outside the confidence interval of the predictions; green dashed line, Fig. 8.4a) cause a slight tailing in the normal QQ-plot (Fig. 8.4c). Moreover, a weak heteroscedastic pattern (Fig. 8.5d) can be recognized and three samples show a big leverage (Fig. 8.4e). However, the Shapiro-Wilk-test (W= 0.946, p= 0.12) and the Kolmogorov-Smirnov-test (D= 0.148, p= 0.46) conducted on the residuals show that the residuals most likely originate from a normal population and, thus, making inferences with the presented calibration model is valid.

The $RABD_{590\text{-}730}$-inferred green pigment concentrations mapped on the sediment-core picture and the time series show an increasing trend and an enhanced seasonal and interannual variability towards the top of the sediment core (Fig. 8.5). Initially, green pigment concentrations show low values (~100-120 µg g^{-1}) and small short-term fluctuations (range +/- 25 µg g^{-1}) from the bottom to ca. ~38 cm (ca. 1800 - 1937). Thereafter, the concentrations as well as the seasonal variability start to increase towards the top of the core, first with a marked but short-lived peak at 26 cm depth (ca. 1958). Maximum values that are significantly above the mean are observed in the top 21.5 cm (1964 to 2015), where seasonal variations in the green pigment concentrations are typically up to 200 µg g^{-1} and interannual variations may be as high as 800 µg g-1 to 1400 µg g^{-1} in years with exceptional algal blooms. A decrease is observed between ~8-4 cm depth (1993 - 2001). After the flood in 2002, values again rapidly increase to earlier maxima (300-530 µg g^{-1} or even 800 µg g^{-1}). Green pigment concentrations are typically low in clastic event layers.

We interpret the overall trends in the HSI-inferred green pigment concentrations as an increase in the net primary productivity (NPP) towards present times. NPP was generally very low from the 1800s to ca. 1937. A slight increase in NPP is observed up to the 1960s. After 1964, significant eutrophication and peak NPP are observed, which continues up to today. A long-term decreasing trend since the 1990s is not found. In contrast, the decrease in the 1990s is followed by a sharp increase in the last decade. The highest green pigment concentrations by year are at 26 cm (1958), 17.5 cm (1973), 10.5 cm (1988), 8 cm (1993), and 2 cm depth (2009).

8.3.4 Sedimentary pigment stratigraphy and fluxes

Changes in the sedimentary pigment stratigraphy (Fig. 8.6a) and fluxes (Fig. 8.6b) reveal information about changes in the trophic state or the algal community, and also serve as an independent control of the HSI data. The CONISS-analysis resulted in three significant (b-stick model) zones.

Zone I (70-40.3 cm, ca. 1800-1937). This zone is characterized by low pigment concentrations overall and by extremely low variability. This is consistent with very low $RABD_{590\text{-}730}$ values and NPP.

Zone II (40.3-21.5 cm; 1937-1964). This zone reveals strong positive trends by a factor of 5 – 10 for the indicators of aquatic NPP (*ββ*-carotene, chlorophyll *a* and pheophytin *a*), and higher pigment concentrations and fluxes overall than Zone I. The trends are particularly strong from 1950 onwards. The TC/CD-ratio (total carotenoids / chlorophyll derivates; here *ββ*-carotene vs. pheophytin *a*) abruptly increases at the bottom of Zone II and stabilizes at high values towards Zone III. As suggested by a decrease in biogenic Si, we interpret these results as a general increase in aquatic NPP and a shift towards more abundant cyanobacteria at the expenses of diatoms. The clastic event layers show low pigment concentrations. Zone III (21.5-0 cm; 1964-2015). This zone shows the highest pigment concentrations and fluxes. The high fluxes of chlorophyll *b*, which are not correlated with the fluxes of chlorophyll *a*, are noteworthy. Chlorophyll *a*, pheophytin *a*, and *ββ*-carotene fluctuate around high levels, decrease after 1993 until 2006, and then steeply increase around 2009 to reach maximum levels in the last decade. *ββ*-carotene, chlorophyll *a* and pheophytin *a* fluxes reach local maxima around 1968, 1987, and the years following 2009. The TC/CD-ratios stay rather constant at high levels, although they drop slightly after 2000 and increase again after 2009. We characterize

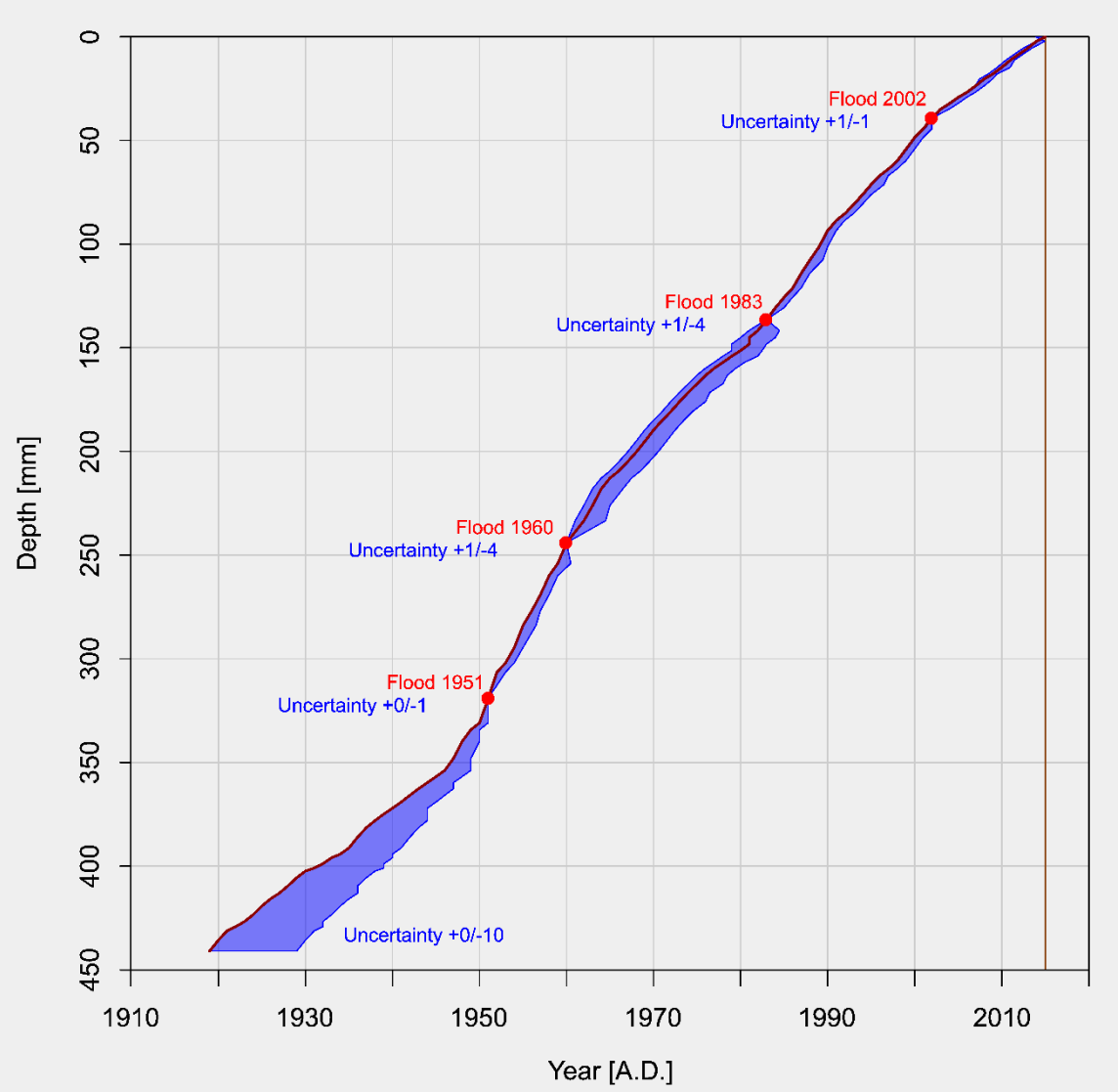

Fig. 8.3 Chronology. The figure shows the varve-chronology of the top 45 cm of the Ponte Tresa sediments. The red dots mark documented flood layers, the dark red line represents the age model, the blue shades represent the estimated errors, and the brown vertical line indicates the coring year (2015).

Zone III as a eutrophic period with very high NPP. Although NPP started to decrease after 1990, values rapidly increased after 2009. The HSI-inferred green pigment concentrations reflect these trends and also show that, after 2009, the NPP increased again.

In general, chlorophyll *a* and pheophytin *a* dominate the sedimentary pigment composition throughout the sediment core, and follow a similar increasing trend. The ratio between 'green pigments' and chlorophyll derivates GP/CD ({chlorophyll *a* + pheophytin *a*}/pheophytin *a*) increases slightly and steadily towards the top of the core (Fig. 8.6b). The comparison between the HPLC-measured pigment stratigraphy and the $RABD_{590\text{-}730}$ inferred 'green pigment' concentrations shows that decadal- and subdecadal trends are very comparable. This is further supported with similar trends seen between RABD-derived 'green pigment' fluxes and chlorophyll *a* fluxes or pheophytin *a* fluxes (Fig. 8.6b), and Pearson-correlations of r= 0.92 (chlorophyll *a* and RABD, ESM Fig. 8.3) and r= 0.96 (pheophytin *a* and RABD, ESM Fig. 8.3). The highly resolved HSI dataset uncovers seasonal and interannual variability, with exceptionally intense algal blooms and extreme NPP at short temporal intervals.

8.4 Discussion

8.4.1 Performance of the HSI-index calibration model

It is essential to ground-truth and verify remotely sensed data with independent established and quantitative analytical methods to properly interpret spectral indices (Butz et al. 2015). Our case study from the Ponte Tresa sediments shows that a calibration between HSI-index data (here: $RABD_{590\text{-}730}$), and

absolute 'green pigment' concentrations {chlorophyll *a* + pheophytin *a*} measured with HPLC, reveals remarkable calibration statistics (R2 = 0.82; RMSEP ~ 12%) and that the methodology developed by Butz et al. (2015) is applicable elsewhere in a different limno-geological setting.

Our calibration model performed better than the one presented in the first case study from Lake Jaczno (Butz et al., 2017, R2 = 0.74, RMSEP ~ 13%). We attribute this improvement to three modifications in the calibration methodology: one in the RABD-calculation, a second one in the subsampling procedure and a third one in the pigment analysis. Firstly, here we used the local minimum of the absorption feature for each individual spectrum, instead of using a fixed band for the trough minimum (Butz et al. 2017). Consequently, small spectral shifts of the trough minimum could be addressed correctly. Secondly, as pointed out in Amann et al. (2014), Butz et al. (2015) and Wirth et al. (2013), it is crucial to have a 'perfect' spatial-match (geo-referencing) between the sampling regions for the non-destructive scanning methods (i.e. the spectral index values calculated thereof) and the sampling regions for the destructive methods (pigment extraction and HPLC), particularly in sediments with spatially highly variable concentrations of the target substances. This is certainly the case for varved sediments, where bioturbation is absent and the seasonal cycles of sediment formation is pronounced. If the sediments are very finely varved, as was the case in Lake Jaczno (Butz et al. 2017), mixed samples of several consecutive varve years had to be taken. This, in turn, resulted in a narrower range of the calibration model as many data points with seasonal or annual maximum pigment concentrations fell outside the calibration range. The varves in our case study are very thick. That enabled precise subsampling of individual extreme seasons with very high pigment concentrations. Thus, the range of our calibration model included >98 % of all HSI-index values in the entire sediment core. Thirdly, in contrast to Butz et al. (2017), who calculated the 'green pigment' concentrations from UV-VIS photometer data, we used HPLC here to quantify specific sedimentary pigment concentrations for calibration with HSI data.

8.4.2 Combination of HPLC- and HSI- inferred pigment concentrations

The key for sub-varve analysis are spatially highly resolved measurements (Wirth et al. 2013). However, the quantitative analytical methods (e.g. HPLC) are mostly limited in the sampling resolution and, hence, intra-annual or inter-annual variability is smoothed out. In contrast to the HPLC-derived sub-decadally resolved pigment stratigraphy (Fig. 8.6), HSI resolves (sub)seasonal variability and extremes of 'green pigment' formation related to individual short-lived algal blooms (Figs. 8.2 and 8.5). It should be noted that the range and validity of the calibration model is fundamental to making full use of the very high spatial resolution (up to 40 x 40 µm pixel size) provided by the hyperspectral imaging method. This opens the door to the analysis of sub-varve scale of NPP. That is clearly an advantage compared with reflectance spectra from point measurements with typical 2-8 mm spatial resolution (Rein and Sirocko 2002; von Gunten et al. 2009; von Gunten et al. 2012; Saunders et al. 2012; Amann et al. 2014; Michelutti and Smol 2016).

However, HSI is much less specific than HPLC. This is because it measures the "bulk" green pigments. Moreover, further specification of spectrally overlapping pigments is not (yet) possible. Consequently, the interpretation of HSI data remains limited. HPLC, in contrast, enables advanced interpretations and is very specific in terms of pigment specification and quantification (depending on the pigment-standards availability). We advocate the combination of both HSI and HPLC methods to enable the interpretation of intra-annual fluctuations as well as the detection of long-term trends in pigment composition and ratios, which is necessary for eutrophication history reconstructions.

8.4.3 Trophic history of the Ponte Tresa basin

Here we present an overview of the trophic development of the Ponte Tresa basin that is based on the well-constrained varve chronology 1919 to 2015. Züllig (1982) already found that the sediment in the Ponte Tresa basin is anoxic and organic-rich, and that sedimentary pigments are well-preserved. This is crucial to interpreting sedimentary pigments as proxies for environmental change (Reuss et al. 2005). Low pigment-fluxes and low TC/CD-ratios measured in Zone I reveal that the period prior to 1937 (upper boundary of Zone I) was characterized by low NPP in an oligotrophic-mesotrophic environment (Swain 1985). The high bSi concentrations indicate the dominance of silicifying algae (particularly diatoms) in Zone I, which was also found by Züllig (1982). That compares well with the investigations of Lotter (2001), who found evidence for oligo- to mesotrophic conditions in Ponte Tresa basin prior to 1935 denoted in the dominance (~70% of diatom assemblage) of Cyclotella diatoms.

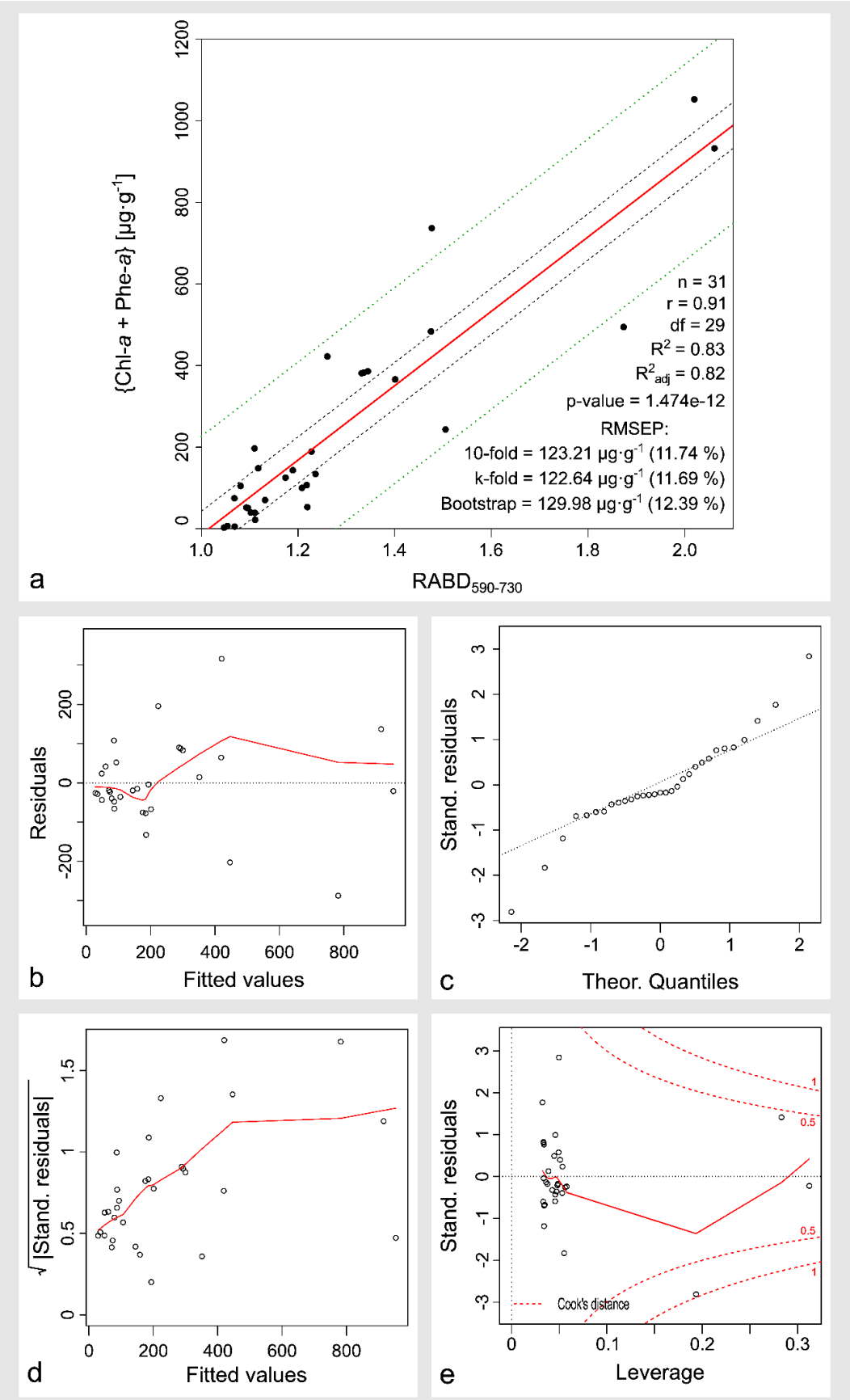

Fig. 8.4 Calibration of $RABD_{590\text{-}730}$ with green pigment concentrations. (a) The linear regression model is shown in red, the black dots indicate the 31 samples, the dashed lines show the 95% confidence intervals for the regression function (black) and the predicted values (green). Different residual plots are shown in (b) residuals vs. fitted values, (c) standardized residuals vs. theoretical quantiles (normal Q-Q plot), (d) scale-location plot, and (e) standardized residuals vs. leverage plot.

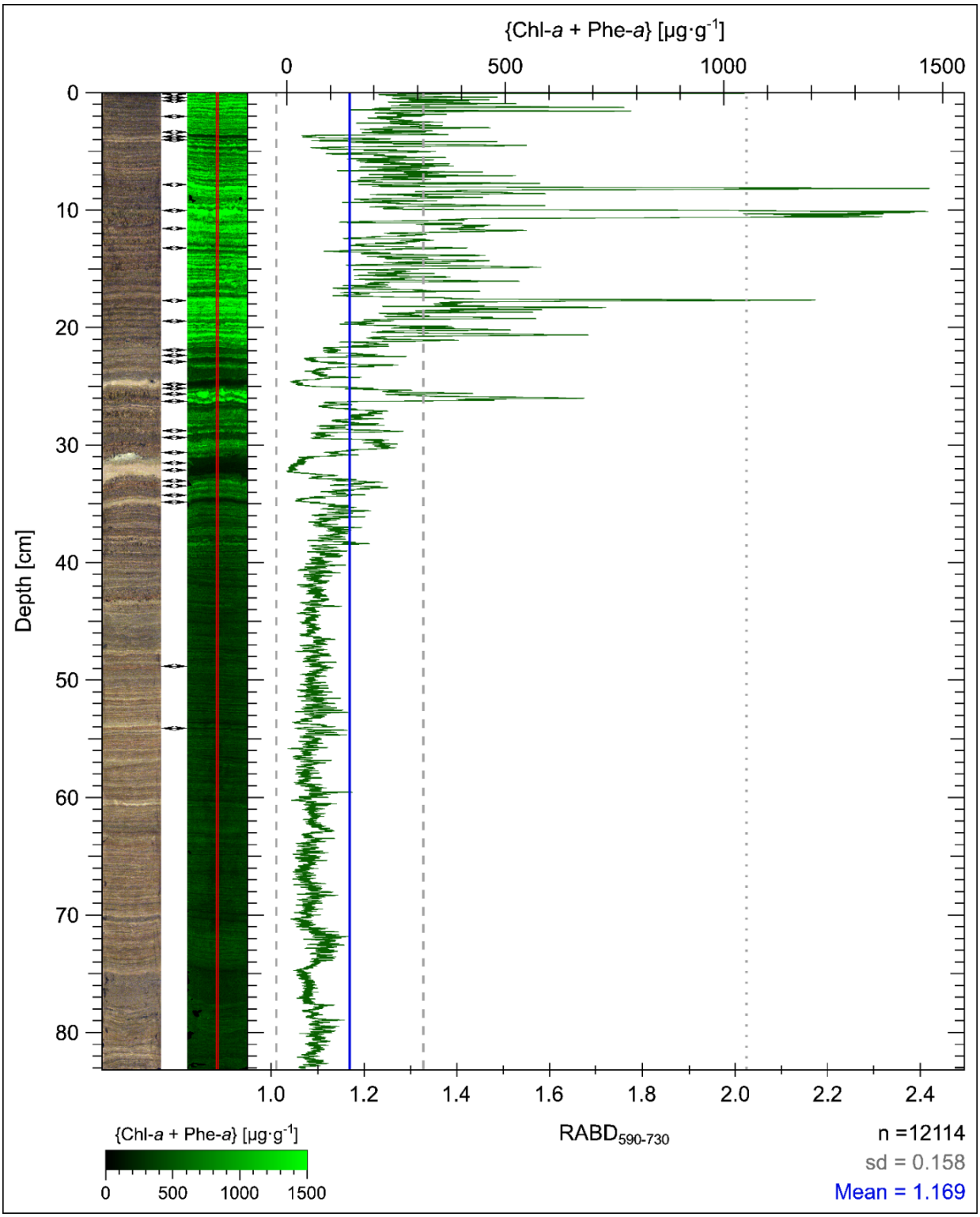

Fig. 8.5 HSI-inferred pigment distribution. The figure shows an RGB contrast enhanced sediment core picture aligned with the distribution map of the green pigment concentrations and the plot of the $RABD_{590\text{-}730}$ index values (bottom scale) and predicted concentrations (top scale). The black arrows indicate the 31 samples used for the calibration. The red line shows the 2 mm wide window which was integrated for the calculation of the time series. The blue line indicates the mean index value and the grey dashed lines represent the standard deviations. The grey dotted line indicates the maximum concentration included in the calibration. The colorbar represents the concentrations of the distribution map.

In Zone II (start ~1937-1964, Fig. 8.6), increasing pigment fluxes, higher TOC values and the increased TC/CD ratio reflect enhanced NPP and substantial eutrophication. This increase in NPP is most likely caused by the combination of the epilimnetic warming that has been observed (Lepori and Roberts 2015), and rapidly increasing external P-loads originating from anthropogenic waste waters between 1940 and 1986 (BAFU 1995). The lower bSi concentrations, along with the higher TC/CD ratio in the 1960s, suggest a shift in the algal composition towards more cyanobacteria at the expenses of diatoms. This is also typical for eutrophication (Swain 1985) and may be related to less transparency in the photic zone and more competition for light (Amann et al. 2014). Indeed, Lotter (2001) found a decrease in Cyclotella diatoms and an increase in Fragilaria, Asterionella and Stephanodiscus parvus diatoms in the Ponte Tresa basin, which he interpreted as a change towards nutrient-enriched conditions starting after 1940. Eutrophication and epilimnetic warming also enhanced the precipitation of authigenic calcite in early summer, the formation of clearly distinguishable varves, and seasonal (or even prolonged) hypolimnetic anoxia. Better formation and preservation of biogeochemical varves as a result of progressive eutrophication has been observed globally (Jenny et al. 2013).

Finally, Zone III (1964 - 2015, Fig. 8.6) shows the highest sedimentary pigment fluxes and TOC concentrations (ESM Fig. 8.1), which is the result of highly eutrophic to hypertrophic conditions. This is also seen in the dominance (~60%) of the Stephanodiscus parvus (typically reflecting hypertrophic conditions) between 1970 and 2000 (Lotter 2001). The increase in chlorophyll *b* can result from algae (Euglenophyta and Chlorophyta) which would indicate eutrophic conditions and/or erosion in the watershed (Leavitt and Hodgson 2002). Seasonal or prolonged lack of oxygen in the hypolimnion has been observed since the middle of the 20th century (Simona 2003), and Niessen (1987) documented the formation of sapropel. The (weak) decrease in pigment fluxes to the sediment between ca. 1988 and 2008 reflects sewage treatment implementation (which started in the 1970s), the ban on P in detergents (which occurred in 1986), and, is also related to enhanced grazing activity and the food web in the oxygenated waters (Barbieri and Simona 2001; Lepori and Roberts 2017).

Despite the general decrease in the external P-loads to Lake Lugano, it is interesting to note that the lake has seen a new boost in pigment fluxes, an increase in the TC/CD ratio and, generally, more eutrophic conditions in the last decade (starting in ~2009). Bottom water oxygen measurements in the southern basin of Lake Lugano (Figino station, 90 m depth) show that, repeated deep mixing started in 2009 and persisted in the following years after a prolonged period of stagnation (2006-2009) (IST-SUPSI 2016). As pointed out by Veronesi et al. (2002) substantial internal recycling of nutrients during periods of deep mixing have apparently increased the PP in the Ponte Tresa basin in recent years. This was later also shown for the holomixis events in the northern basin of Lake Lugano in 2005 and 2006 (Lepori and Roberts 2017). We think that similar processes have triggered the algal blooms in 1958, 1973, 1988 and 1993 (extremes in the $RABD_{590\text{-}730}$ values, Fig. 8.6a).

8.5 Conclusions

Hyperspectral imaging is a novel non-destructive, very high-resolution and rapid technique which, in combination with other methods and proxies, provides information about sub-varve scale variability, trends and extremes of 'green pigment' concentrations in lake sediments. This is an important basis to assess the historical context of lacustrine eutrophication. However, the applicability of the hyperspectral imaging method needs to be tested in different limno-geological settings. From our case study in the Ponte Tresa basin, Lake Lugano, we draw the following conclusions: The methodological design for the calibration of the hyperspectral data with HPLC-inferred data is fundamental for the performance of the calibration model. We propose first to evaluate the spatial distribution of the spectral index values (here the values for $RABD_{570\text{-}730}$) along the sediment core and, afterwards, to select the regions of interest for sediment subsampling (for subsequent HPLC analysis) accordingly. Ideally, the calibration samples are taken with a stratified sampling along the full gradient of the spectral index values (pigment concentrations), including the maxima and minima. Sampling of the maxima is particularly important to quantify the pigment concentrations for short-lived events (such as e.g. algal blooms) from high-resolution (µm-scale) hyperspectral data. The good performance of our calibration model (R2=0.82, RMSEP ~12%, >98% of all spectral index values are included in the calibration range) and the very high spatial resolution of the pixel size (68 µm x 68 µm) demonstrates the potential of hyperspectral imaging techniques for the geochemical analysis of lake sediments. Combined with specific pigment data inferred e.g. from HPLC analysis, hyperspectral imaging data provide information about the historical context of eutrophication at very high

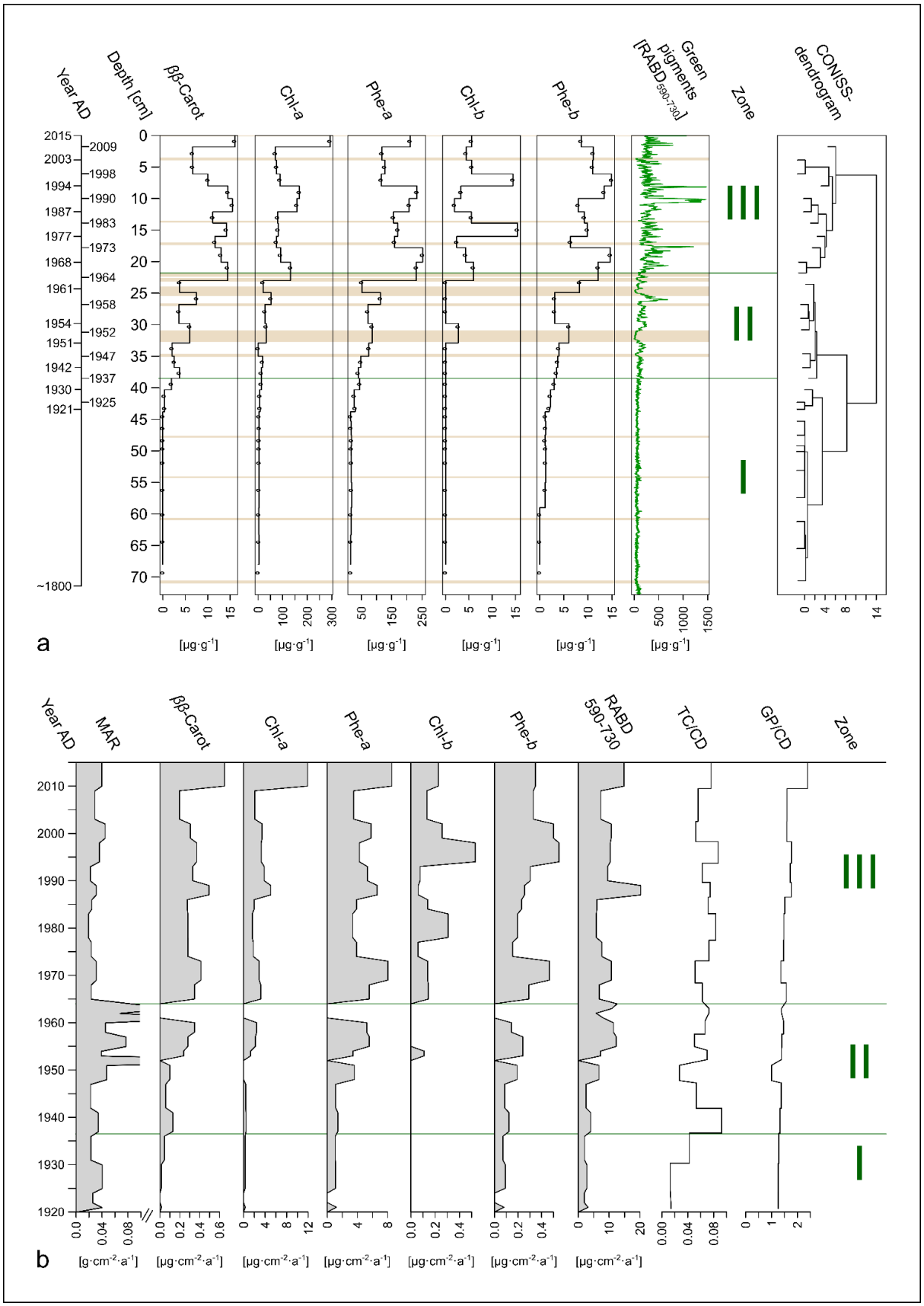

Fig. 8.6 Pigment stratigraphy of the Ponte Tresa sediment core. (a) The pigment stratigraphy based on the measured concentrations. An excerpt of the varve-chronology is shown on the left side. "Green pigments" represent the HSI-inferred pigment concentrations. The green horizontal lines separate the three significant clusters retrieved by the CONISS analysis. The CONISS-dendrogram is shown on the right side. Brown shades highlight flood layers. (b) The MAR and pigment fluxes are shown from 1919 to 2015. $RABD_{590\text{-}730}$ represents the HSI-inferred pigment fluxes linearly approximated to the sampling resolution of the other pigments. The green horizontal lines again indicate the three significant CONISS-clusters.

seasonal and interannual resolution (subvarve- and varve-scale resolution). In the Ponte Tresa basin, very low levels of primary production ({chlorophyll *a* + pheophytin *a*} <50 µg g^{-1}) and very small interannual variability persisted in an oligotrophic to mesotrophic lake between ca. 1800 and the 1930s. From the 1930s to 1964, a clear increase in pigment concentrations and pigment fluxes, but also interannual variability was noted, and a first extreme algal bloom was observed in 1958. Primary productivity peaked between the late 1960s and the early 1990s with very high interannual variability and multiple prominent algal blooms, and extreme concentrations of sedimentary green pigments {chlorophyll *a* + pheophytin *a*} of up to 1400 µg g^{-1} were observed. In the following years, and as a result from restoration measures to remove external P-loads, eutrophication levels decreased slightly until ca. 2009. Despite ongoing reduction of external P-loads, the last decade (2009-2015) has again seen maximum levels of pigment fluxes to the sediment. This is attributed to efficient internal P-cycling related to repeated deep convection and vertical mixing in the lake.

8.6 Acknowledgements

The project was funded by the Swiss National Science Foundation grant 200021_152986. MG designed the research. DR, CB and TS did all the sedimentological and statistical analyses. TS and MG wrote the paper, all authors commented on the drafts. We thank Dr. Daniela Fischer for the lab assistance and Carole Adolf (Institute of Plant Sciences, University of Bern) for the support in the field and the varve counting.

8.7 References

Aeschbach-Hertig W, Holzner CP, Hofer M, Simona M, Barbieri A, Kipfer R (2007) A time series of environmental tracer data from deep meromictic Lake Lugano, Switzerland. Limnol Oceanogr 52:257–273. doi: 10.4319/lo.2007.52.1.0257

Airs RL, Atkinson JE, Keely BJ (2001) Development and application of a high resolution liquid chromatographic method for the analysis of complex pigment distributions. J Chromatogr A 917:167–177. doi: 10.1016/S0021-9673(01)00663-X

Amann B, Lobsiger S, Fischer D, Tylmann W, Bonk A, Filipiak J, Grosjean M (2014) Spring temperature variability and eutrophication history inferred from sedimentary pigments in the varved sediments of Lake Żabińskie, north-eastern Poland, AD 1907-2008. Glob Planet Change 123:86–96. doi: 10.1016/j.gloplacha.2014.10.008

Barbieri A, Simona M (2001) Trophic evolution of Lake Lugano related to external load reduction: Changes in phosphorus and nitrogen as well as oxygen balance and biological parameters. Lakes Reserv Res Manag 6:37–47. doi: 10.1046/j.1440-1770.2001.00120.x

Battarbee RW, Bennion H, Gell P, Rose N (2012) Ecosystems. In: Matthews JA, Bartlein PJ, Briffa KR, Dawson AG, de Vernal A, Denham T, Fritz SC, Oldfield F (eds) The SAGE Handbook of Environmental Change: Volume 2: Human Impacts and Responses, 1st edn. SAGE Publications Inc., London, pp 583–606

Blass A, Bigler C, Grosjean M, Sturm M (2007) Decadal-scale autumn temperature reconstruction back to AD 1580 inferred from the varved sediments of Lake Silvaplana (southeastern Swiss Alps). Quat Res 68:184–195. doi: 10.1016/j.yqres.2007.05.004

Boehrer B, Schultze M (2008) Stratification of lakes. Rev Geophys 46:1–27. doi: 10.1029/2006RG000210

Bundesamt für Umwelt (BAFU) (1995) Der Zustand der Seen in der Schweiz.

Bundesamt für Umwelt (BAFU) (2016) Faktenblatt: Der Lago di Lugano. Zustand bezüglich Wasserqualität. Bern

Butz C, Grosjean M, Goslar T, Tylmann W (2017) Hyperspectral imaging of sedimentary bacterial pigments: a 1700-year history of meromixis from varved Lake Jaczno, northeast Poland. J Paleolimnol 58:57–72. doi: 10.1007/s10933-017-9955-1

Butz C, Grosjean M, Fischer D, Wunderle S, Tylmann W, Rein B (2015) Hyperspectral imaging spectroscopy: a promising method for the biogeochemical analysis of lake sediments. J Appl Remote Sens 9:1–20. doi: 10.1117/1.jrs.9.096031

Conley DJ, Schelske CL (2002) Biogenic Silica. In: Smol JP, Birks HJB, Last WM (eds) Tracking Environmental Change Using Lake Sediments. Volume 3: Terrestrial, Algal, and Siliceous Indicators. Kluwer Academic Publishers, Dordrecht, pp 289–293

Croudace IW, Rindby A, Rothwell RG (2006) ITRAX: description and evaluation of a new multi-function X-ray core scanner. In: Rothwell RG (ed) New Techniques in Sediment Core Analysis, special Publication. Geological Society, London, pp 51–63

Croudace IW, Rothwell RG (2015) Micro-XRF Studies of Sediment Cores: A Perspective on Capability and Application in the Environmental Sciences. doi: 10.1007/978-94-017-9849-5_1

Das B, Vinebrooke RD, Sanchez-Azofeifa A, Rivard B, Wolfe AP (2005) Inferring sedimentary chlorophyll concentrations with reflectance spectroscopy: a novel approach to reconstructing historical changes in the trophic status of mountain lakes. Can J Fish Aquat Sci 62:1067–1078. doi: 10.1139/f05-016

Dean W (1999) The carbon cycle and biogeochemical dynamics in lake sediments. J Paleolimnol 21:375–393.

Friedrich J, Janssen F, Aleynik D, Bange HW, Boltacheva N, Çagatay MN, Dale AW, Etiope G, Erdem Z, Geraga M,

Gilli A, Gomoiu MT, Hall POJ, Hansson D, He Y, Holtappels M, Kirf MK, Kononets M, Konovalov S, Lichtschlag A, Livingstone DM, Marinaro G, Mazlumyan S, Naeher S, North RP, Papatheodorou G, Pfannkuche O, Prien R, Rehder G, Schubert CJ, Soltwedel T, Sommer S, Stahl H, Stanev EV, Teaca A, Tengberg A, Waldmann C, Wehrli B, Wenzhöfer F (2014) Investigating hypoxia in aquatic environments: Diverse approaches to addressing a complex phenomenon. Biogeosciences 11:1215–1259. doi: 10.5194/bg-11-1215-2014

Grimm EC (1987) CONISS: a FORTRAN 77 program for stratigraphically constrained cluster analysis by the method of incremental sum of squares. Comput Geosci 13:13–35. doi: 10.1016/0098-3004(87)90022-7

Guilizzoni P, Marchetto A, Lami A, Gerli S, Musazzi S (2011) Use of sedimentary pigments to infer past phosphorus concentration in lakes. J Paleolimnol 45:433–445. doi: 10.1007/s10933-010-9421-9

Håkanson L, Jansson M (2002) Principals of Lake Sedimentology. The Blackburn press, Caldwell, New Jersey

Hall R, Leavitt P, Smol J, Zirnhelt N (1997) Comparison of diatoms, fossil pigments and historical records as measures of lake eutrophication. Freshw Biol 38:401–417. doi: 10.1046/j.1365-2427.1997.00251.x

Heiri O, Lotter AF, Lemcke G (2001) Loss on ignition as a method for estimating organic and carbonate content in sediments: reproducibility and comparability of results. J Paleolimnol 25:101–110. doi: 10.1023/A:1008119611481

Huser BJ, Egemose S, Harper H, Hupfer M, Jensen H, Pilgrim KM, Reitzel K, Rydin E, Futter M (2016) Longevity and effectiveness of aluminum addition to reduce sediment phosphorus release and restore lake water quality. Water Res 97:122–132. doi: 10.1016/j.watres.2015.06.051

Istituto scienze della Terra (IST-SUPSI) (2016) Ricerche sull'evoluzione del Lago di Lugano. Aspetti limnologici. Programma quinquennale 2013-2015. Campagna 2015 e sintesi pluriennale.

Jenny JP, Arnaud F, Dorioz JM, Giguet Covex C, Frossard V, Sabatier P, Millet L, Reyss J-L, Tachikawa K, Bard E, Pignol C, Soufi F, Romeyer O, Perga M-E (2013) A spatiotemporal investigation of varved sediments highlights the dynamics of hypolimnetic hypoxia in a large hard-water lake over the last 150 years. Limnol Oceanogr 58:1395–1408. doi: 10.4319/lo.2013.58.4.1395

Jenny JP, Francus P, Normandeau A, Lapointe F, Perga M-E, Ojala A, Schimmelmann A, Zolitschka B (2016) Global spread of hypoxia in freshwater ecosystems during the last three centuries is caused by rising local human pressure. Glob Chang Biol 22:1481–1489. doi: 10.1111/gcb.13193

Juggins S (2017) rioja: Analysis of Quaternary Science Data, R package version 0.9-15.

Kamatani A, Oku O (2000) Measuring biogenic silica in marine sediments. Mar Chem 68:219–229. doi: 10.1016/S0304-4203(99)00079-1

Kassambara A, Mundt F (2017) factoextra: Extract and Visualize the Results of Multivariate Data Analyses, R package version 1.0.4.

Korhola A, Sorvari S, Rautio M, Appleby PG (2002) A multi-proxy analysis of climate impacts on the recent development of subarctic Lake Sannajärvi in Finnish Lapland. J Paleolimnol 28:59–77.

Kruse FA, Boardman JW, Huntington JF (1999) Fifteen years of hyperspectral data: Northern Grapevine Mountains, Nevada. Proc. 8th JPL Airborne Earth Sci. Work. Jet Propulsion Laboratory Publication, pp 247–258

Lami A, Guilizzoni P, Marchetto A (2000) High resolution analysis of fossil pigments, carbon, nitrogen and sulphur in the sediment of eight European Alpine lakes: the MOLAR project. J Limnology 59:15–28. doi: 10.4081/jlimnol.2000.s1.15

Larsson LA (2003) Cybis CooRecorder - Image Coordinate Recording program.

Leavitt PR, Hodgson DA (2002) Sedimentary Pigments. In: Smol JP, Birks HJB, Last WM (eds) Tracking Environmental Change Using Lake Sediments. Volume 3: Terrestrial, Algal, and Siliceous Indicators. Kluwer Academic Publishers, Dordrecht, pp 295–325

Lee M, Shevliakova E, Malyshev S, Milly PCD, Jaffé PR (2016) Climate variability and extremes, interacting with nitrogen storage, amplify eutrophication risk. Geophys Res Lett 43:7520–7528. doi: 10.1002/2016GL069254

Lepori F, Roberts JJ (2017) Effects of internal phosphorus loadings and food-web structure on the recovery of a deep lake from eutrophication. J Great Lakes Res 43:255–264. doi: 10.1016/j.jglr.2017.01.008

Lepori F, Roberts JJ (2015) Past and future warming of a deep European lake (Lake Lugano): What are the climatic drivers? J Great Lakes Res 41:973–981. doi: 10.1016/j.jglr.2015.08.004

Lotter AF (2001) The effect of eutrophication on diatom diversity: examples from six Swiss lakes. In: Jahn R, Kocioleck JP, Witkowski A, Compère P (eds) Lange-Bertalot-Festschrift. Ruggel, Gantner, pp 417–432

Meyers PA (1994) Preservation of elemental and isotopic source identification of sedimentary organic matter. Chem Geol 114:289–302.

Michelutti N, Smol JP (2016) Visible spectroscopy reliably tracks trends in paleo-production. J Paleolimnol 56:253–265. doi: 10.1007/s10933-016-9921-3

Mills K, Schillereff D, Saulnier-Talbot É, Gell P, Anderson NJ, Arnaud F, Dong X, Jones M, McGowan S, Massaferro J, Moorhouse H, Perez L, Ryves DB (2017) Deciphering long-term records of natural variability and human impact as recorded in lake sediments: a palaeolimnological puzzle. Wiley Interdiscip Rev Water 4:e1195. doi: 10.1002/wat2.1195

Niessen F (1987) Sedimentologische, geophysikalische und

geochemische Untersuchungen zur Entstehung und Ablagerungsgeschichte des Luganersees (Schweiz). Mitteilungen aus dem geologischen Institut der eidg. Technischen Hochschule und der Universität Zürich, Institut der Eidg. Technischen Hochschule und der Universität Zürich, Zürich, pp 332

Nordmeyer, H, Lanzetta, L, Nicollin, B (1978) Bathymetric map of Lake Lugano. European Community Information Service.

Ohlendorf C, Sturm M (2008) A modified method for biogenic silica determination. J Paleolimnol 39:137–142.

Palmisano DF (2008) Ponte Tresa, Terra ed Acque: Documenti per una storia del territorio., Edizioni A. Ponte Tresa. Archivo storico di Ponte Tresa CH, Vol.7. Ponte Tresa, pp 300

R Core Team (2016) R: A Language and Environment for Statistical Computing.

Rein B, Lückge A, Reinhardt L, Sirocko F, Wolf A, Dullo WC (2005) El Niño variability off Peru during the last 20,000 years. Paleoceanography 20:1-17. doi: 10.1029/2004PA001099

Rein B, Sirocko F (2002) In-situ reflectance spectroscopy - analysing techniques for high-resolution pigment logging in sediment cores. Int J Earth Sci 91:950–954. doi: 10.1007/s00531-002-0264-0

Reuss N, Conley DJ, Bianchi TS (2005) Preservation conditions and the use of sediment pigments as a tool for recent ecological reconstruction in four Northern European estuaries. Mar Chem 95:283–302. doi: 10.1016/j.marchem.2004.10.002

Salmaso N, Morabito G, Garibaldi L, Mosello R (2007) Trophic development of the deep lakes south of the Alps: a comparative analysis. Fundam Appl Limnol / Arch für Hydrobiol 170:177–196. doi: 10.1127/1863-9135/2007/0170-0177

Sanger JE (1988) Fossil pigments in paleoecology and paleolimnology. Palaeogeogr Palaeoclimatol Palaeoecol 62:343–359. doi: 10.1016/0031-0182(88)90061-2

Saunders KM, Kamenik C, Hodgson DA, Hunziker S, Siffert L, Fischer D, Fujak M, Gibson JAE, Grosjean M (2012) Late Holocene changes in precipitation in northwest Tasmania and their potential links to shifts in the Southern Hemisphere westerly winds. Glob Planet Change 92–93:82–91. doi: 10.1016/j.gloplacha.2012.04.005

Schillereff DN (2015) A review of in situ measurement techniques for investigating suspended sediment dynamics in lakes. Geomorphol Tech (Online Ed) Br Soc Geomorphol London 3:1–12.

Schnurrenberger D, Russell J, Kelts K (2003) Classification of lacustrine sediments based on sedimentary components. J Paleolimnol 29:141–154. doi: 10.1023/A:1023270324800

Schultheiss PJ, Weaver PPE (1992) Multi-sensor Core Logging For Science And Industry. In: Dorman CE (ed) OCEANS 92 Proceedings: Mastering the Oceans Through Technology., 2nd edn. IEEE, Newport, pp 608–613

Simona M (2003) Winter and spring mixing depths affect the trophic status and composition of phytoplankton in the northern meromictic basin of Lake Lugano. J Limnol 62:190–206. doi: 10.4081/jlimnol.2003.190

Smith VH (1998) Cultural eutrophication of inland, estuarine, and coastal waters. Successes, limitations, Front. Ecosyst. Sci. Springer, pp 7–49

Swain EB (1985) Measurement and interpretation of sedimentary pigments. Freshw Biol 15:53–75.

Tylmann W, Bonk A, Goslar T, Wulf S, Grosjean M (2016) Calibrating 210Pb dating results with varve chronology and independent chronostratigraphic markers: Problems and implications. Quat Geochronol 32:1–10. doi: 10.1016/j.quageo.2015.11.004

Veronesi ML, Barbieri A, Hanselmann KW (2002) Phosphorus, carbon and nitrogen enrichment during sedimentation in a seasonally anoxic lake (Lake Lugano, Switzerland). J Limnol 61:215–223. doi: 10.4081/jlimnol.2002.215

von Gunten L, Grosjean M, Kamenik C, Fujak M, Urrutia R (2012) Calibrating biogeochemical and physical climate proxies from non-varved lake sediments with meteorological data: Methods and case studies. J Paleolimnol 47:583–600. doi: 10.1007/s10933-012-9582-9

von Gunten L, Grosjean M, Rein B, Urrutia R, Appleby P (2009) A quantitative high-resolution summer temperature reconstruction based on sedimentary pigments from Laguna Aculeo, central Chile, back to AD 850. The Holocene 19:873–881. doi: 10.1177/0959683609336573

Wirth SB, Gilli A, Niemann H, Dahl TW, Ravasi D, Sax N, Hamann Y, Peduzzi R, Peduzzi S, Tonolla M, Lehman MF, Anselmetti FS (2013) Combining sedimentological, trace metal (Mn, Mo) and molecular evidence for reconstructing past water-column redox conditions: The example of meromictic Lake Cadagno (Swiss Alps). Geochim Cosmochim Acta 120:220–238. doi: 10.1016/j.gca.2013.06.017

Zolitschka B, Francus P, Ojala AEK, Schimmelmann A (2015) Varves in lake sediments - a review. Quat Sci Rev 117:1–41. doi: 10.1016/j.quascirev.2015.03.019Züllig H (1982) Untersuchungen über die Stratigraphie von Carotinoiden im geschichteten Sediment von 10 Schweizer Seen zur Erkundung früherer Phytoplankton-Entfaltungen. Schweizerische Zeitschrift für Hydrol 44:1–98. doi: 10.1007/BF02502191

8.8 Supplementary material

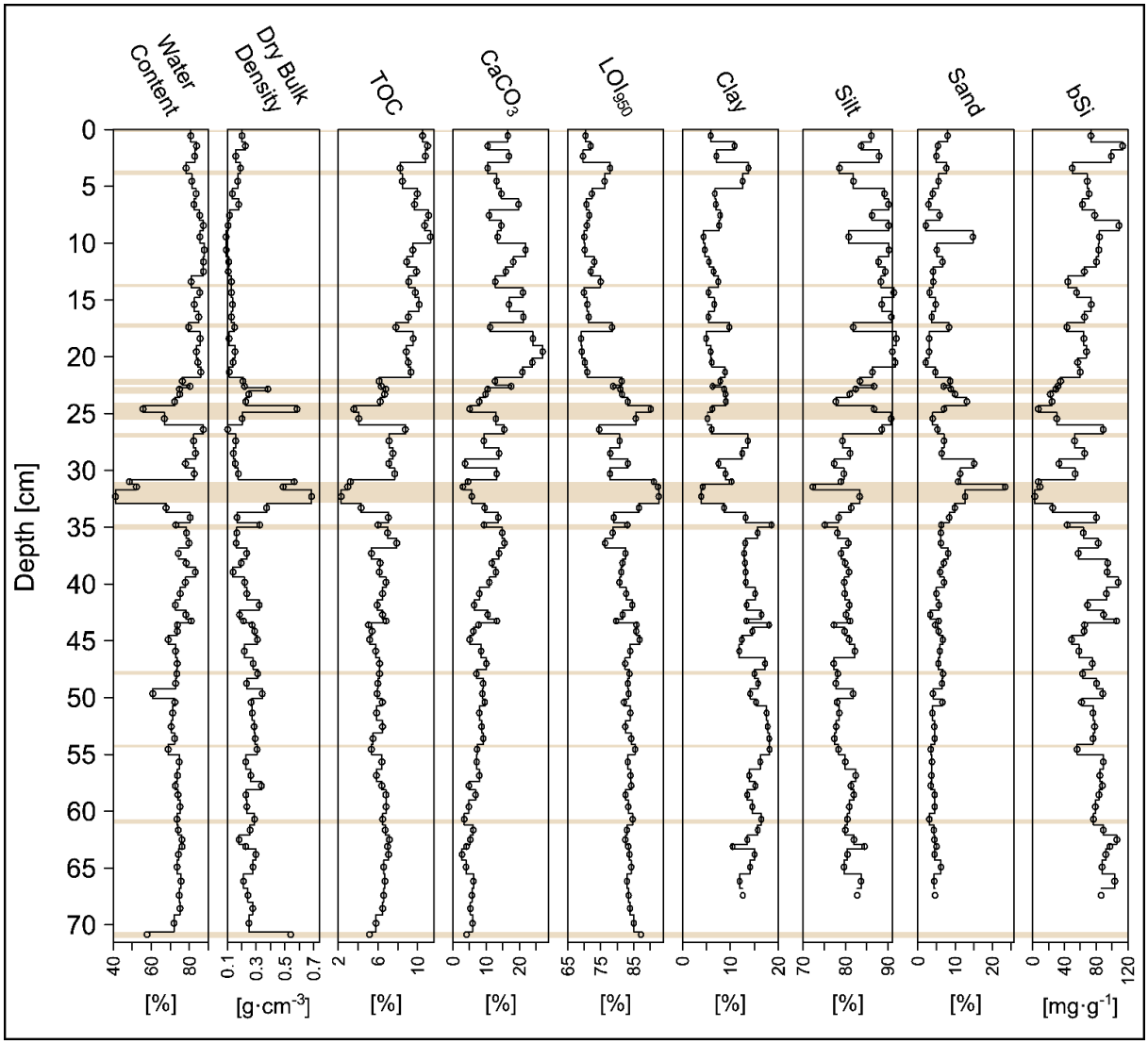

ESM Fig. 8.1 Stratigraphy of different measured geochemical proxies (concentrations). The brown shades represent the flood layers.

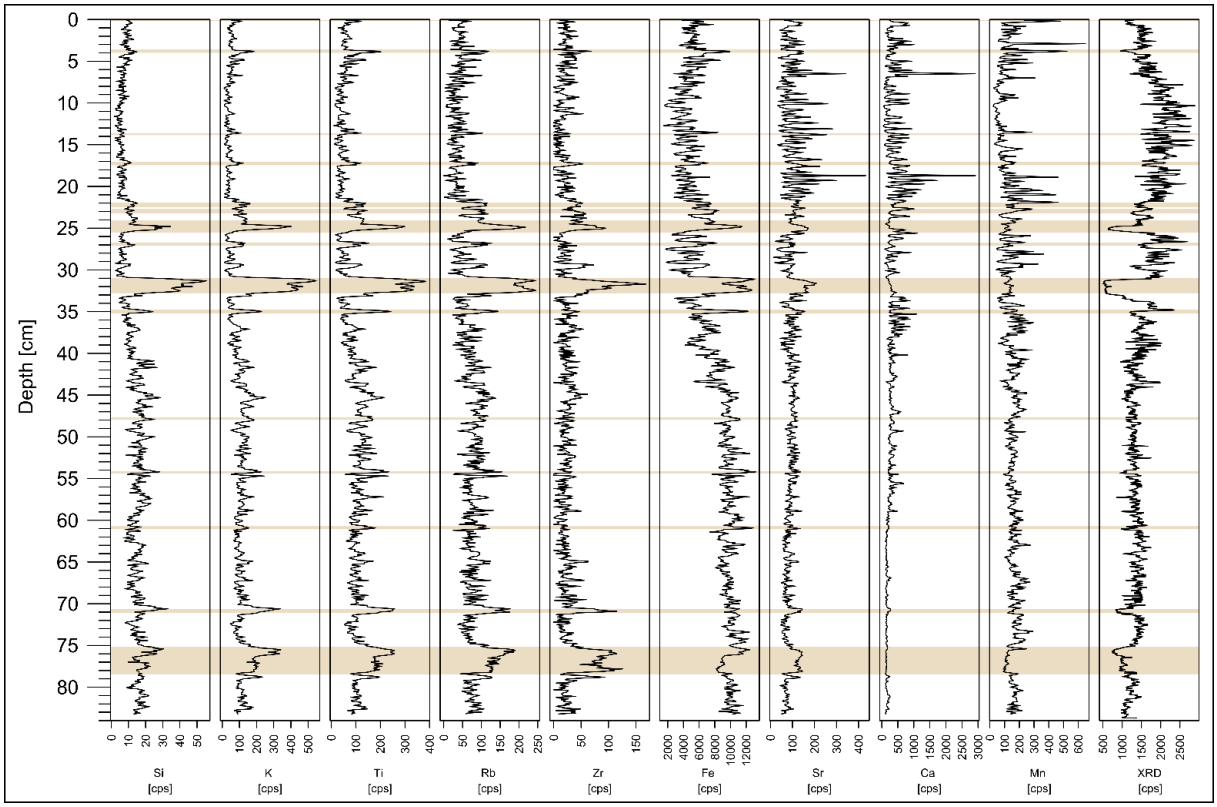

ESM Fig. 8.3 XRF-data. Elemental counts are represented in counts per second (adjusted for exposure time of 20s). RAD refers to radio-density, the radio-denser the material, the lower the counts. The brown shades represent the flood layers.

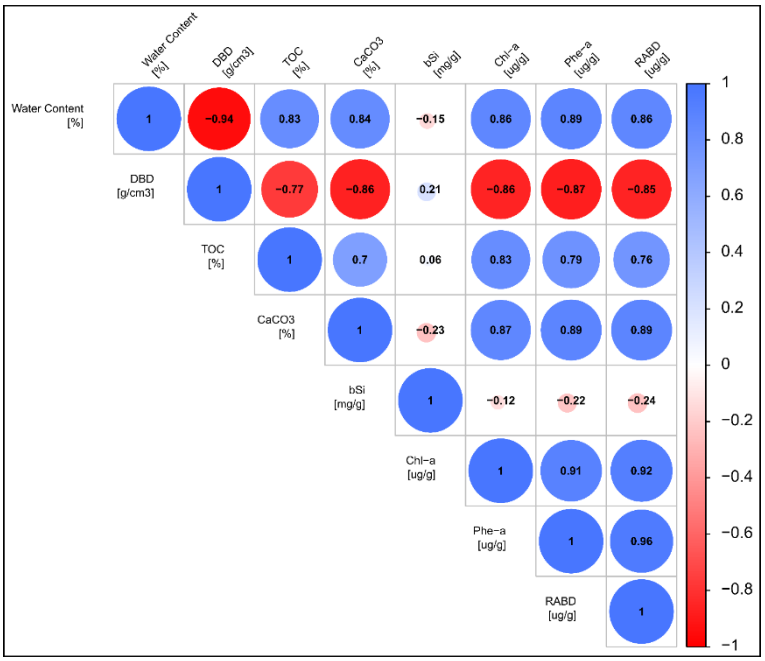

ESM Fig. 8.2 Correlation matrix of organic proxies and pigment data measured by HPLC and HSI. The sampling resolution of the pigments (presented in Fig. 8.6) was used. In total 29 samples (complete) points are included. The proxy-order follows the output of hierarchical clustering.